Influence of Rotational Stiffness Modeling on the Joint Behavior of Quasi-Rectangular Shield Tunnel Linings

Weixi Zhang [1] , Wouter De Corte [1,*] , Xian Liu [2] and Luc Taerwe [1,2]

[1]   Department of Structural Engineering and Building Materials, Ghent University, 9000 Ghent, Belgium; Weixi.Zhang@UGent.be (W.Z.); Luc.Taerwe@UGent.be (L.T.)

[2]   College of Civil Engineering, Tongji University, Shanghai 200092, China; xian.liu@tongji.edu.cn

*   Correspondence: Wouter.DeCorte@UGent.be

check for updates

Featured Application: (1) In quasi-rectangular tunnels, a new type of special-section shield tunnels, the effect of nonlinear joint behavior is much more important than in circular tunnels. (2) An iterative nonlinear spring-beam model for the prediction of lining deformations and bending moments in a shield tunnel is presented. (3) The predictions are validated against unique full ring test results. (4) The relevance of the presented method, compared to a constant joint stiffness approach, is demonstrated. (5) A parametric study into the design parameters for quasi-rectangular tunnels is presented.

Abstract: A beam-spring model with constant rotational stiffness is a practical tool for the prediction of the general deformations and bending moments in circular tunnel linings. However, in reality, the rotational stiffness of a segmental joint is not constant, due to nonlinear deformations and local yielding in the vicinity of the joint. These are a result of the specific geometry at the joint, which is related to water-tightness measures and buildability issues. For quasi-rectangular tunnels this nonlinearity should not be neglected, as the bending component in the lining is significantly larger compared to circular linings. To date, there are only few studies that have investigated a calculation method for consideration of the joint's nonlinear moment-axial force and shear-axial force interaction behavior and its consequences on the calculated lining behavior. In this paper, an iterative incremental method is proposed to tackle this issue, based on rotational stiffness curves derived from 3D nonlinear finite element modelling of the joints, and substantiated by testing. The significance of the variable rotational stiffness is highlighted through a comparison with results based on a constant stiffness assumption. Further, using the proposed calculation method, the effects of the circumferential joints, the bending moment transmission and several other parameters on the full-ring behavior of quasi-rectangular tunnels are discussed for a wide interval of design parameters. The results provide some new insights into the behavior of this non-traditional tunnel type. Although the presented results are related to specific overall and local geometries, the presented method is considered to be useful for the design of other special tunnel geometries.

Keywords: iterative incremental method; quasi-rectangular shield tunnel; joint behavior; experimental validation; parametric study

1. Introduction

When a shield tunnel is constructed, the choice of a suitable cross-section for the tunnel is very important, especially when the tunnel is built in a city center. Compared to traditional circular

tunnels, the quasi-rectangular shield tunnel with improved cross-sectional shape, makes two-way subway transportation in one tube possible, as shown in Figure 1. This concept can reduce both the construction costs and the environmental impact. Moreover, when compared to a large-diameter circular shield tunnel, the underground space efficiency can be increased by 20%, and the buried depth can be decreased significantly [1–3]. Compared to other special-section shield tunnels, the following advantages of a quasi-rectangular tunnel are emphasized: easier control of the surface subsidence when compared to that of a double-O tube (DOT) in relation to improper backfilling grouting and the concave shape of the shield machine [4,5], and the low cost of the segment linings due to the use of reinforced concrete compared to the composite steel-concrete segments in the rectangular cross-section tunnels in Rokujizo Station, the Ishida Station, and Hongqiao Linkong 11-3 Connection [6,7]. Given the above, quasi-rectangular shield tunnels are expected to be used for a wide range of applications in the future.
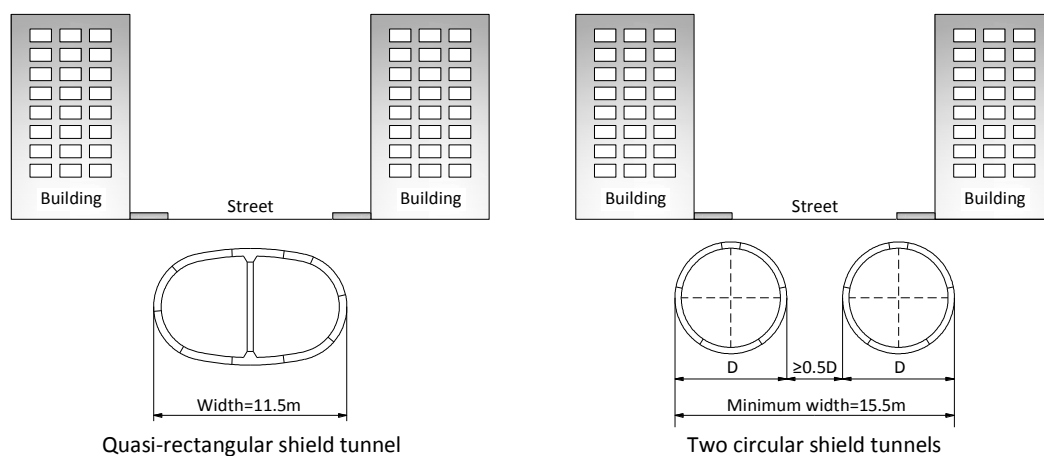

Figure 1. Comparison of two circular single track shield tunnels and a quasi-rectangular double track shield tunnel.

At present, the basic design principles for quasi-rectangular tunnels linings are identical to those for circular tunnels. Research related to calculation models for special-section tunnel linings is rarely published. To date, four types of calculation methods for tunnel linings can be used in practice: (a) the routine method, which fully ignores the effect of the segmental joints [8]; (b) the multi-hinge ring method, which treats the joints as free hinges [9]; (c) the modified routine method (MRM), which assumes an average uniform rigidity ring based on a rigidity reduction factor and bending moment transmission [10,11]; (d) the beam-spring model (BSM), which treats the segments as beams and the joints as springs [12,13]. Methods (a) and (b) cannot reflect the real structural behavior and are therefore not commonly used. Although the MRM method relies much on empirical parameters and the BSM method requires defining accurate spring parameters through experience, tests, analytical solution or numerical analysis, these two types are used widely in practice [12]. Furthermore, other calculation approaches have been developed in recent decades. Analytical solutions for circular and DOT tunnels considering the effects of joint stiffness are established by Lee et al. [14] and Hu et al. [15] respectively. However, only symmetric load distributions or anti-symmetric load distributions are possible for the analytical solutions. For cast-iron segmental tunnels, a 3D tunnel model in which the joint bolts are replaced by a set of springs is developed, and a good agreement between the 3D model and field measurements is achieved [16,17]. A heterogeneous equivalent beam model is proposed, converting the local range of joints into a beam element according to the actual stress state on the joint section and then treating the non-continuous segment linings as a continuous heterogeneous structure [18]. It is obvious that all these models focus on how to deal with the joints, especially with the rotational behavior of the longitudinal joints.

Indeed, given the existence of the longitudinal and circumferential joints, segmental linings are a non-continuous structure. The effects of the joints on internal forces and lining displacements are significant and should be carefully taken into account in the design [14,19–21]. In previous studies, the rotational stiffness of lining joints was considered as a constant parameter [14,22,23]. However, many studies and experiments have shown that there are a number of influential factors on the rotational stiffness in longitudinal joints, such as their inability to transfer tensile stress, the different section sizes, the number of bolts, the bolt pretightening forces and the structural geometries [24–26]. The rotational stiffness is also related to the level of internal forces, including both axial forces and bending moments [26,27], which we define in this paper as moment-axial force interaction behavior. A bilinear or multi-linear constitutive relation to describe moment-axial force interaction behavior of the various joints is introduced based on experiments or numerical approaches [28–30]. Although the moment-axial force interaction behavior of longitudinal joints is recognized [20,31], research about the calculation method on how to fully consider this joint characteristic in the full ring calculations and the related effect is rarely found, especially on special-section tunnels where this is more relevant.

The related studies [32,33] have observed the moment-axial force characteristic of the joints in quasi-rectangular tunnels. However, Liu et al. [32] presented full-scale ring experiments and focused on the bearing mechanism and failure process of the overall lining structure, whereas Zhang et al. [33] validated a 3D joint model by comparing results from model to experiments. How to take account of the joints' moment-axial force characteristic into the general structural model and its effect on the structural behavior were not further studied. Moreover, also the shear stiffness of the joint in quasi-rectangular tunnels varies with the joint's axial forces, which we define in this paper as shear-axial force interaction behavior. Since relatively larger bending moments and shear forces occur in special-shaped shield tunnels compared to those in circular tunnels [34], the joints' moment-axial force and shear-axial force interaction behavior should be given appropriate attention. On the other hand, the sizes of the segments in quasi-rectangular tunnels are restricted by the narrow assembly space in the tunnel boring machine, so the joints are arranged much closer. It means that the influence of the joints on the overall structural performance may be larger than in other shield tunnels. All these factors make the effect of the joints' moment-axial force and shear-axial force interaction behavior non-negligible.

In this paper, an iterative incremental beam-spring model is used to consider the stiffness variation caused by moment-axial force and shear-axial force interaction behavior for each joint. The precise model parameters are derived from a nonlinear 3D finite element analysis of the local joint behavior and from the results of joint experiments. The iterative model is verified by an indoor full-scale ring experiment, and the significance of the joints' nonlinear interaction behavior is emphasized through a comparison between the results from the proposed iterative model and models with constant joint stiffness. Finally, for this new type of tunnel, the presented model reveals some unique aspects of quasi-rectangular linings. These aspects can be of relevance in further quasi-rectangular tunnel applications and are a possible reference for other special-section tunnels.

2. Model Setup

2.1. Introduction of the Quasi-Rectangular Tunnel Concept

The quasi-rectangular shield tunnel is a new alternative for shield driven tunnels in urban railway transportation systems and was first used in Line 3 of the metro transit system in Ningbo, China. Figure 2 shows an outline of a typical lining structure of the quasi-rectangular shield tunnel. The structure is composed of ten segments and an interior column, in a configuration with overall outside dimensions of 11.50 × 6.94 m. The thickness and width of the segments are 450 and 1200 mm, respectively, while these of the interior column are 350 and 700 mm. The cross-section of the quasi-rectangular tunnel considered in this paper, consists of four arcs, two of 24 degrees with a 15.45 m radius and two of 156 degrees with a 3.20 m radius.

The concrete grade of the lining structure is C50 (characteristic cube compressive strength of 50 MPa) and the steel quality is HRB400 (characteristic yield stress of 400 MPa) according to the Chinese Code for Design of Concrete Structures [GB50010] [35]. The tunnel construction adopts a staggered assembly, with pattern A and pattern B linings, which are symmetrical with respect to the interior column. In each longitudinal joint, two pairs of cast iron embedded parts serve as connections, and each pair is connected by two 6.8-M33 (tensile stress of 600 MPa, yield stress of 480 MPa, diameter of 33 mm) short straight bolts [1,7].
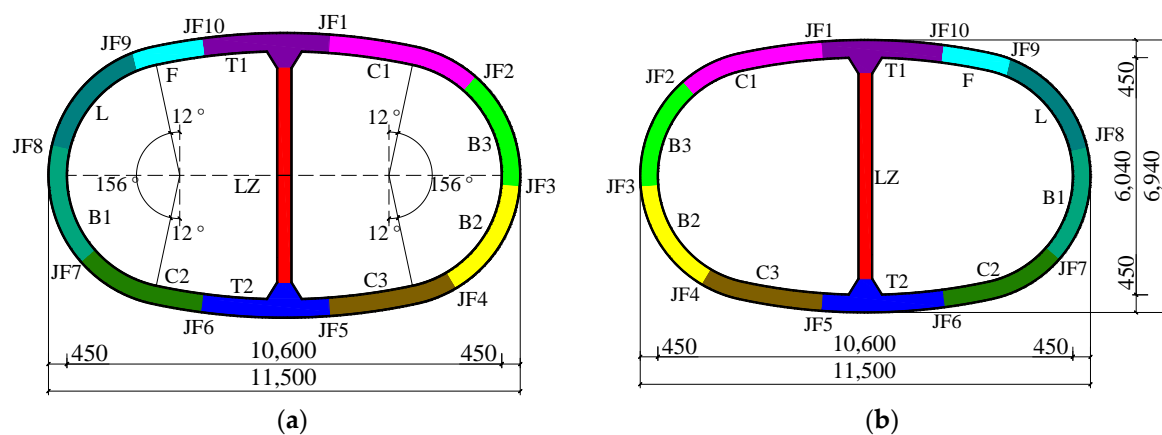
Figure 2. Outline of a typical lining structure of the Ningbo quasi-rectangular tunnel (unit: mm): (**a**) pattern A; (**b**) pattern B.

2.2. Model Establishment

2.2.1. General Concept

As mentioned previously, the MRM and BSM methods are the most commonly used calculation methods for shield tunnels in practice. Unfortunately, the MRM method requires a number of empirical parameters, which have to be determined by experience. Moreover, this method does not allow for the precise calculation of the actual distribution of the bending moments [13–15]. Since the BMS method seems the most promising approach, its applicability in special-section tunnels is investigated in this paper.

As the tunnel construction adopts a staggered assembly, with alternating linings of pattern A and pattern B, the calculation model applied in the current research contains three rings: a front half ring (Pattern B), a middle full ring (Pattern A) and a back half ring (Pattern B). In this way, the effect of the neighboring lining structures is simulated with a minimum length for this kind of staggered assembly. We consider the joints between the segments in one ring as longitudinal joints, and the joints between the neighboring rings as circumferential joints. As shown in Figure 3, both rotational and radial shear springs are considered in the longitudinal joints, while radial and tangential shear springs are considered in the circumferential joints. The segments and columns are simplified as beam elements, with areas and moments of inertia determined according to their specific size and amount of reinforcement.

2.2.2. Spring Elements

Accurate prediction of joint deformations is important, as it influences the overall structural deformations and consequently the overall internal forces to a great extent. Controlling the structural deformations is an essential performance assessment index, which often governs the thickness of the lining structure.
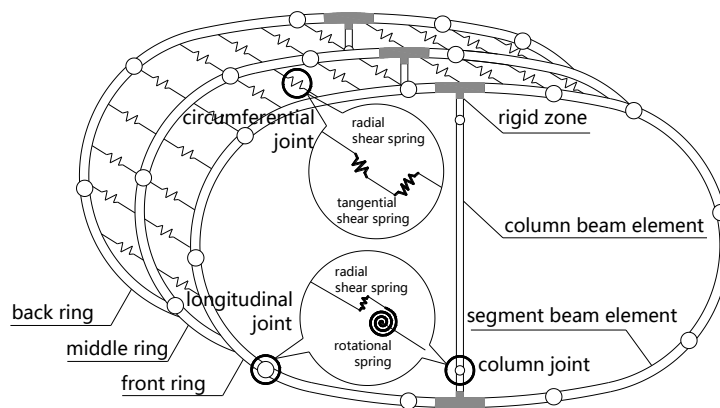
Figure 3. Beam-spring model of the quasi-rectangular shield tunnel linings.

Traditionally, in the BSM method, the spring element is given a fixed stiffness value, or given fixed positive and negative stiffness values for all joints. However, the joint's rotational stiffness value varies under different combinations of bending moments and axial forces, and additionally, the joint's shear stiffness value is also affected by the acting compressive forces. Examples of such behavior are given in Section 2.3.1.

The spring used in this paper is a unidirectional element, with a nonlinear generalized force-displacement capability. It has longitudinal or torsional functions in three degrees of freedom. The longitudinal capability is a uniaxial tension-compression function and the torsional capability is a purely rotational function. In a state of plain strain, this spring element consists of a pair of nodes, which are at the same spatial position, as shown in Figure 4. Each node has three degrees of freedom, i.e., two translational modes and one rotational mode, all in plane. K_θ, K_n and K_s, respectively, represent the rotational, tangential and radial stiffness. In the current case, a rotational spring and a translational spring are considered in the longitudinal joints and two translational springs in different directions in the circumferential joints.
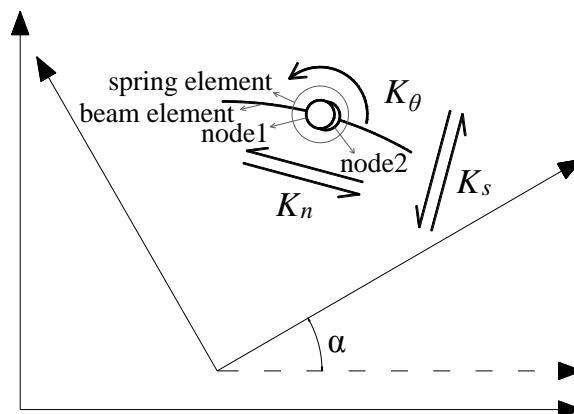

Figure 4. Illustration of a general spring element.

2.2.3. Rigid Zones

The T-shaped segments (T1 and T2 in Figure 2) have a transition function to connect the neighboring segments with the interior column, which does not exist in circular tunnels. A concept of rigid connection is proposed in the model. A proper method to consider the mechanical properties of this area is needed, similar to the calculation of a column and beam joint in frame structure buildings. As such, this concept is introduced into the quasi-rectangular tunnel model and its effects will be discussed later. Based on the Chinese Technical Specification for Concrete Structure of Tall Building [JGJ3-2010] [36], an illustration of the rigid zone is shown in Figure 5 and its size can be determined

through expressions (1), (2) and (3). Herein, b_c is the average thickness of the haunch (the top and bottom thicknesses of the haunch are 850 and 350 mm, then b_c equals 600 mm) and h_b is the thickness of the segment (450 mm). Two rigid zones are introduced at the upper and lower T-shaped segments with the following characteristics.

$$l_{h1} = 0.5b_c - 0.25h_b, \tag{1}$$

$$l_{h2} = 0.5b_c - 0.25h_b, \tag{2}$$

$$l_{c1} = 0.5h_b - 0.25b_c. \tag{3}$$

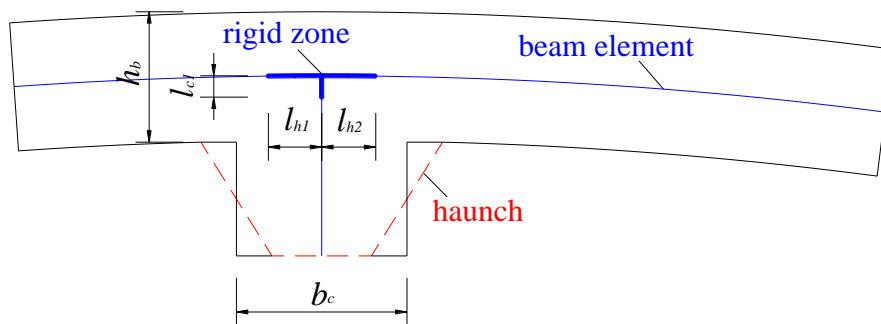This results in $l_{h1} = l_{h2} = 187.5$ mm and $l_{c1} = 75$ mm.

Figure 5. Illustration of the characteristics of the rigid zone.

2.2.4. Full-Ring Model Calculation

In the full-ring model, rotational stiffness and radial shear stiffness are considered for the longitudinal joints while radial shear stiffness and tangential shear stiffness are considered for the circumferential joints. The stiffness matrix is $K = [K_{l\theta}, K_{ls}, K_{cn}, K_{cs}]$ with $K = [K_{l\theta1}, K_{l\theta2}, \cdots, K_{l\theta12}]$ representing the rotational stiffness matrix of the moment-rotation curves of the longitudinal joints JF1 to JF12, $K_{ls} = [K_{ls1}, K_{ls2}, \cdots, K_{ls12}]$ representing the radial shear stiffness matrix for the longitudinal joints JF1 to JF12, $K_{cn} = [K_{cn1}, K_{cn2}, \cdots, K_{cnn}]$ representing the tangential shear stiffness matrix of the circumferential joints, $K_{cs} = [K_{cs1}, K_{cs2}, \cdots, K_{csn}]$ representing the radial shear stiffness matrix of the circumferential joints. The number of springs in the circumferential joints can be defined as needed. The positions of the joints, key sections (JM) and key deformation points (ends of line segments D) for the structure are shown in Figure 6.
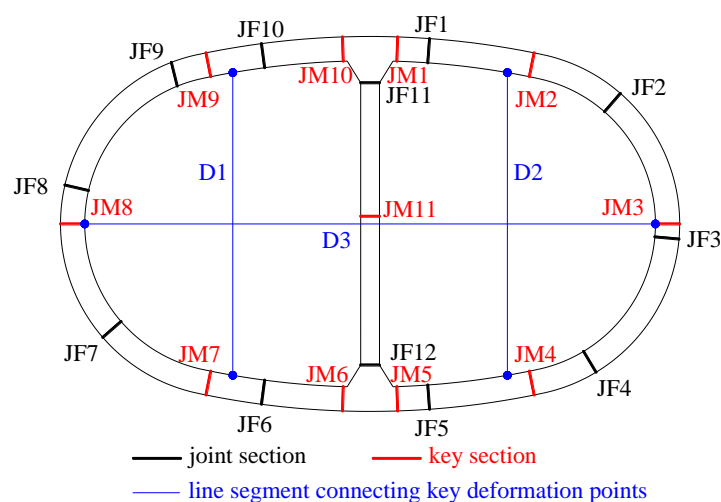

Figure 6. Key sections and deformation points for the model calculation.

The key sections, except for JM11, are the sections with a relatively large bending moment, which will be decisive for the reinforcement area in the corresponding segments. JM11 experiences a large axial force rather than bending moment and is selected as a key section to represent the stress condition in the interior column. The key deformation points are used to calculate the structural convergence deformation. This convergence deformation is the relative deformation of a pair of specific measurement points. For circular or quasi-rectangular tunnels, the measurement points are usually selected at the ends of the axes crossing, the center of the circular section horizontally and vertically. Positive values correspond to outward deformations, while negative values correspond to inward deformations. According to the Chinese Code for Design of Metro [GB50157] [37], this convergence deformation should be maximum 3‰ of the corresponding axis length. This means that the deformations of D1, D2 and D3 should be maximum 3‰ of the lengths of D1, D2 and D3, respectively.

2.3. Joint Parameters: Establishment of Joint Parameter Database

2.3.1. Introduction

In large special-section shield tunnels with more than 10-m diameter, a configuration with more longitudinal joints is indispensable to make the segment transportation and manipulation in the assembly feasible. Inevitably, some joints will be at locations where large internal forces exist, such as JF3, JF6, JF8, JF10 (Figure 2). In these joints, the nonlinear behavior will become apparent, affecting the overall lining behavior. On the other hand, due to the existence of the interior column, the shear forces are much larger than commonly found in circular tunnels, affecting the structural convergence deformation to a great extent.

For these reasons, full-scale experiments are necessary to provide straightforward results for the joint's mechanical properties. The results from these joint experiments can support the use of this joint type and provide the necessary input parameters in the lining structure model. A range of full-scale joint experiments, related to the specific joint configuration in the considered quasi-rectangular shield tunnel, was carried out, including bending moment resistance experiments and shear resistance experiments, as shown in Figure 7. All structural details of the actual joint configuration are retained in the test segments, such as grooves for the waterproof belt and positioning rod.

(**a**)	(**b**)

Figure 7. Joint experiments: (**a**) bending moment resistance experiment; (**b**) shear resistance experiment.

2.3.2. Rotational Stiffness

As mentioned previously, full-scale bending moment resistance experiments on longitudinal joints were conducted to investigate the $M - \theta$ curve under different loading conditions. Furthermore, a 3D finite element simulation approach was developed, taking into account the cast iron parts, and the reinforcement in the precast concrete segments. The details of the bending moment resistance experiments and the 3D simulation model are provided in Appendix A. The simulation model provides a verified approach for obtaining the joint's rotation under a given axial force and bending

moment. Numerically predicted and experimentally verified moment-rotation curves, based on the joint configuration of the quasi-rectangular shield tunnel, are presented in Figure 8. The results provide insight into the rotational stiffness for axial forces up to 1200 kN and absolute bending moments up to 400 kNm. There are two categories of bending moments in the segments. One category relates to positive bending moments. These moments create compression at the outer side of the segment and tension at the inner side. The other category relates to negative bending moments, which create the opposite stress distribution. Based on the variation of the joint's opening at the inner and outer side, joint rotations can be calculated by dividing this variation by the total joint height. Clearly, the rotational stiffness decreases with increasing bending moment, and the stiffness changes quickly in the range of bending moments from 100 to 300 kNm. Since the bending moments of many joints occur in this range, as shown in Section 4.2 for a case with a 17 m buried depth, the relevance of the nonlinear approach is evident. In addition, the influence of the axial forces, which increase the rotational stiffness over the full range of bending moments, is also apparent. Considering the fact that different axial forces occur in different joints, one $M - \theta$ curve cannot represent the rotational behavior of all the joints in a quasi-rectangular tunnel lining. Hence a surface function of the joint's rotational behavior is needed. This function should include the axial force and bending moment as variables and cover different axial force and bending moment combinations.
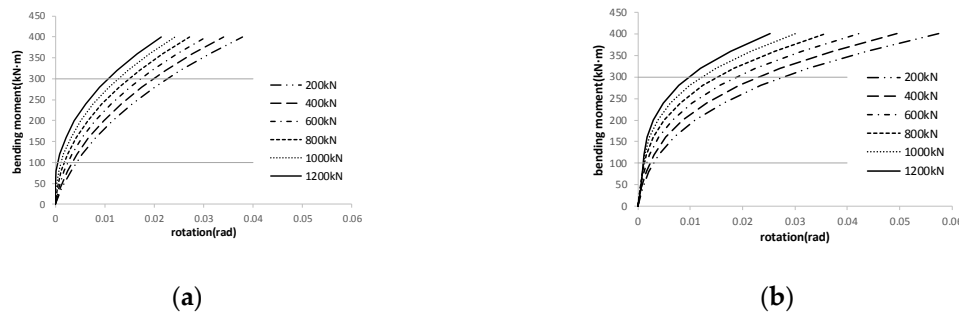

(a)

(b)

Figure 8. Calculated results of bending moment resistance experiments: (**a**) positive moment; (**b**) negative moment.

From the verified numerical model and for the joint geometry of the quasi-rectangular shield tunnel, two surface functions for positive and negative bending moments are derived. These functions are used as an input in the full-ring structural calculations. A cubic polynomial function of bending moment M (unit: kNm) and axial force N (unit: kN) according to Formula (4), can fit the rotations well. The polynomial coefficients corresponding to the best-fitting results are listed in Table 1.

$$\theta(N, M) = a \cdot M^3 + b \cdot M^2 \cdot N + c \cdot M \cdot N^2 + d \cdot M^2 + e \cdot M \cdot N + f \cdot M. \tag{4}$$

Table 1. List of coefficients and goodness of fitting.

Coefficient	Positive	Negative
a	9.33×10^{-11}	6.58×10^{-10}
b	-1.18×10^{-11}	-2.03×10^{-10}
c	8.34×10^{-12}	2.40×10^{-11}
d	1.30×10^{-7}	9.17×10^{-8}
e	-4.80×10^{-8}	-3.29×10^{-8}
f	3.79×10^{-5}	2.36×10^{-5}
SSE	5.116×10^{-6}	1.092×10^{-4}
Adjusted R-square	0.999	0.998

The authors are aware that these values are related to the specific geometry of the quasi-rectangular shield tunnel under consideration but are confident that these can be integrated in a lining joint database

in the future. Such a database could be based on numerical predictions and/or experimental results and could provide a valuable support for lining design. Further, the authors believe that the number of parameters involved in the creation of these values is too large to allow for further simplifications to this approach.

2.3.3. Shear Stiffness

Shear resistance experiments were carried out to investigate the shear behavior of the joints under a combination of shear and axial forces. Two categories of tests were conducted in the shear resistance experiments. If the shear exerted at the joint makes the segment move with a relatively outward tendency, we define this type of shear as outward shear. If the shear exerted at the joint makes the segment move with a relatively inward tendency, we define this type of shear as inward shear. The details of the shear resistance experiments can be found in Appendix B. The results of the shear stiffness tests are shown in Figure 9, where the shear stiffness is calculated by dividing the relative displacement of the two segments beside the joint by the exerted shear force. For convenience, all the calculations regarding the shear resistance are based on the unit length of 1 m. After the normalization into 1 m length, the unit of compressive force is kN/m, while the shear stiffness is expressed in kN/m^2. For the joint geometry of the quasi-rectangular shield tunnel, the results from inward and outward shear experiments are similar. The shear stiffness increases linearly with the compressive force. It is worth noting that the compressive force relates to the axial force in longitudinal joints and to the longitudinal force in circumferential joints.
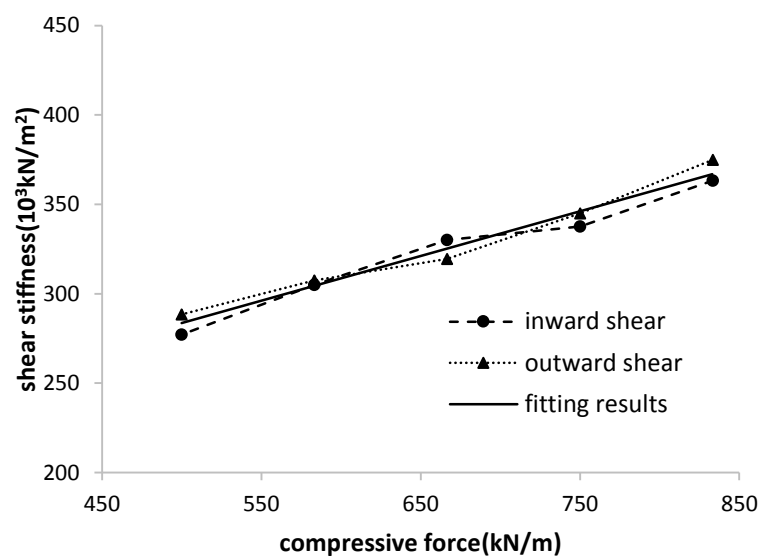

Figure 9. Relationship between shear stiffness and compressive force.

After linear fitting, the following shear stiffness function is obtained:

$$K_{ls} = 0.25N + 158.67, \tag{5}$$

here in N (kN/m) is the compressive force and K_{ls} (10^3 kN/m^2) is the shear stiffness.

3. Comparison between Proposed Full-Ring Model and Experiments

3.1. Full-Scale Ring Experiment

Indoor full-scale ring experiments allow for a direct evaluation of the mechanical performance of tunnel linings. The loads exerted on the structure are clearly defined, and the measurement results from this kind of indoor experiments are relatively reliable when compared to those from an in-situ tunnel.

Full-scale ring experiments have been performed for the Green Heart Tunnel in the Netherlands [38], the Elbe Tunnel in Germany [39], the Shanghai Changjiang Tunnel [40], a water storage and sewage tunnel in Shanghai [41] and special-section tunnels including rectangular tunnels [5] and DOT shield tunnels [3,42].

In this paper, the results from a full-scale ring experiment are used to verify the applicability of the previously presented incremental model. In the test, a full ring is placed horizontally into a self-balancing steel frame (Figure 10a). Every loading point is equipped with two hydraulic jacks with a maximum load output of 2000 kN. A series of steel balls is deployed under the horizontal ring specimen to provide a test condition with negligible friction. During the loading process, 30 loading points are arranged over the circumference to simulate different kinds of loads, such as soil and water pressure and ground overload. These loading points can be divided into several groups for load applications in different experimental cases. All hydraulic jacks in the same group provide an equal load simultaneously.

During the test, the convergence deformations and displacements of the structure are monitored by 46 displacement transducers. The strains on the rebar and concrete are measured by 424 and 224 strain gauges, respectively. Before the formal loading, all loading jacks and measuring meters were calibrated, and a pre-experiment was carried out to eliminate the initial gaps between the segments which might appear during the assembly. After that, an inspection of the bolts was performed to ensure all connections were stable, in order to reduce the initial structural deformation.
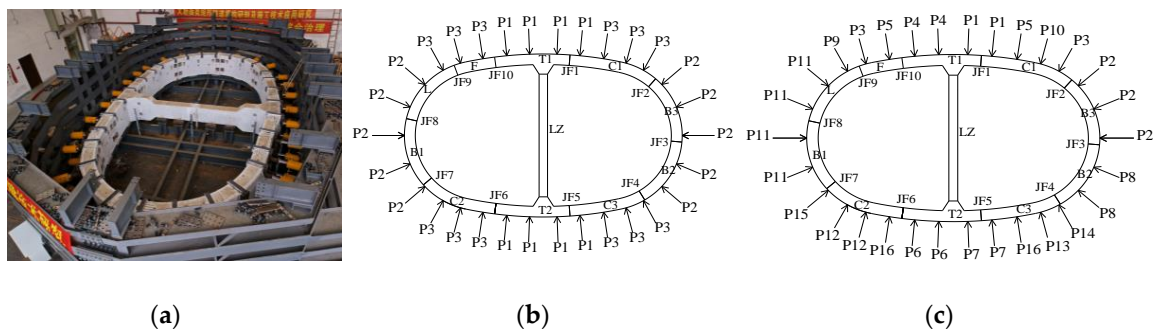

Figure 10. Indoor full-ring experiment: (**a**) loading frame; (**b**) jack distribution for Experimental Cases 1 and 2; (**c**) jack distribution for Experimental Case 3.

Three experimental cases are selected to compare the results from experiments and the aforementioned iterative model. In Experimental Cases 1 and 2, the 30 jacks are divided into 3 groups (Figure 10b) while 16 groups are used to simulate the load distribution in Experimental Case 3 (Figure 10c), in which an extra partial offset pressure on the left half side of 30 kPa is simulated. This corresponds to the relatively dangerous design condition of the tunnel going partially under a building or when new construction is taking place close to an existing tunnel. A summary of the design parameters and the experimental loads are presented in Table 2. The strata surrounding the tunnel is mucky clay and mucky silty clay. The unit weight of the soil is 18 kN/m^3. The water level is 0.5 m below the ground. In order to use the 30 loading points to simulate the design condition, the principles for deciding the groups and values of these loading points include both equivalences of the load distributions on the linings and similarity of the internal forces and deformations between experiment and design. Although the real load exerted on the tunnel and the corresponding structural mechanical behavior cannot be exactly simulated by the 30 point loads due to the complexity of the soil-structure interaction, plenty of preliminary calculations were made to ensure the internal forces of key sections and displacement of key deformation points (in Figure 6) in the tested linings are approximately equivalent to those of an actual tunnel structure under the given design conditions. This principle of soil load simulation through separate point loads was also adopted in previous full-scale ring experiments [3,5,38–40,43,44].

Table 2. Full-scale ring experimental cases.

Experimental Case	Soil Overburden (m)	Coefficient of Lateral Pressure	Ground Overload (kPa)	Experimental Load (kN)
1	8	0.7 (soil-water together)	20 kPa	P1 = 300, P2 = 170, P3 = 212
2	17	0.4 (soil-water separately)	20 kPa	P1 = 450, P2 = 250, P3 = 355
3	17	0.7 (soil-water together)	20 kPa and partial offset load of 30 kPa on left half	P1 = 481, P2 = 227, P3 = 503, P4 = 458, P5 = 344, P6 = 599 P7 = 400, P8 = 486, P9 = 406 P10 = 239, P11 = 255, P12 = 388 P13 = 489, P14 = 40, P15 = 387 P16 = 258

3.2. Comparison of Internal Forces and Deformations

As the point loads in the indoor full-scale ring experiments and the corresponding structural responses are clearly identified, the results from the iterative numerical model under these 30 point loads are compared with those from the experiments.

Based on the measurements and the assumption of plane strain, internal forces at the eleven key sections (See Figure 6) in the experiments are calculated through Formula (6).

$$\begin{cases} N = \int_{-h/2}^{h/2} \sigma[\varepsilon(y)]bdy + \varepsilon_s E_s A_s + \varepsilon'_s E'_s A'_s \\ M = \int_{-h/2}^{h/2} \sigma[\varepsilon(y)]bydy + (\varepsilon_s E_s A_s - \varepsilon'_s E'_s A'_s)(h/2 - c) \end{cases} \tag{6}$$

In the formula, h, b and c represent the thickness of a segment, the width of a segment and the distance from the center of the reinforcement layer to the closest segment edge. $\varepsilon(y)$ refers to the strain of concrete at different positions in the direction of segment thickness, and $\sigma[\varepsilon(y)]$ refers to the concrete stress corresponding to the concrete strain. ε_s, E_s and A_s refer to the strain of the reinforcement close to the external surface of the segment, the elastic modulus of steel and the area size of the corresponding reinforcement while ε'_s, E'_s and A'_s are for the reinforcement close to the internal surface of the segment. The constitutive stress-strain relationship of the concrete is quadratic while that of the steel rebars is considered linear.

The internal forces and deformations from the experiments and the iterative model under the 30 point loads are listed in Table 3, with the ratios of model values to experimental results. From the numerical results, it is found that the errors on the axial forces at most of the key sections are under 5%, while those at the other sections are smaller than 10%. For the bending moments, differences at most of the key sections are within 10%, with the exceptions of the 17% value for JM7 in Experimental Case 1 and 11% value for JM10 in Experimental Case 3.

When it comes to the structural deformations (in Table 4), most of the differences are within the range of 10%, with the exception of the 18% value for D1 in Experimental Case 3. This can be attributed to the small value of convergence deformation of 2.21 mm obtained from the calculation. Moreover, the absolute error measured for this case was only 0.34 mm. To make a direct sense of the structural deformations, the measured displacements at the measuring points in Experimental Case 1 are shown in Figure 11. The red line in Figure 11 is calculated numerically, and the obtained displacements are visualized with a scale factor of 80. Overall, it is found that the calculated deformations from the iterative model and the experimental results are in good agreement.

Table 3. Comparison of internal forces.

Experimental Case	Key Section	Experiment		Model		Ratio (Model/Experiment)	
		Bending Moment (kNm)	Axial Force (kN)	Bending Moment (kNm)	Axial Force (kN)	Bending Moment	Axial Force
1	JM1	−289	−631	−269	−635	0.93	1.01
	JM2	237	−628	231	−602	0.97	0.96
	JM3	−121	−719	−118	−708	0.97	0.99
	JM4	247	−592	234	−601	0.95	1.02
	JM5	−283	−648	−277	−634	0.98	0.98
	JM6	−287	−635	−276	−633	0.96	1.00
	JM7	260	−596	217	−600	0.83	1.01
	JM8	−135	−741	−147	−711	1.09	0.96
	JM9	210	−598	204	−604	0.97	1.01
	JM10	−298	−636	−300	−637	1.01	1.00
	JM11	−9	−1191	−12	−1232	-	1.03
2	JM1	−376	−1024	−357	−972	0.95	0.95
	JM2	364	−929	385	−923	1.06	0.99
	JM3	−230	−1064	−220	−1114	0.95	1.05
	JM4	356	−961	382	−922	1.07	0.96
	JM5	−355	−1044	−369	−971	1.04	0.93
	JM6	−350	−1025	−382	−970	1.09	0.95
	JM7	340	−959	356	−921	1.05	0.96
	JM8	−270	−1003	−261	−1118	0.97	1.11
	JM9	364	−936	354	−926	0.97	0.99
	JM10	−354	−1081	−382	−974	1.08	0.90
	JM11	−63	−2077	−11	−1944	-	0.94
3	JM1	−436	−1140	−401	−1092	0.92	0.96
	JM2	255	−1016	273	−1047	1.07	1.03
	JM3	−103	−1226	−109	−1159	1.06	0.95
	JM4	213	−1088	207	−1053	0.97	0.97
	JM5	−419	−1127	−435	−1095	1.04	0.97
	JM6	−275	−1027	−288	−1088	1.05	1.06
	JM7	417	−1048	396	−1043	0.95	0.99
	JM8	−316	−1251	−331	−1275	1.05	1.02
	JM9	437	−1056	412	−1032	0.94	0.98
	JM10	−352	−1153	−390	−1084	1.11	0.94
	JM11	−79	−1908	−41	−1977	-	1.04

Table 4. Comparison of convergence deformations.

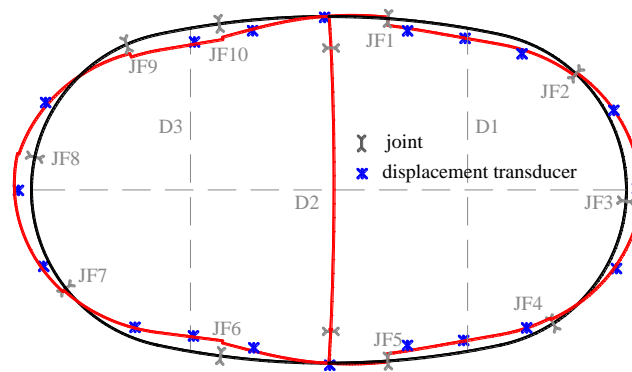| Experimental Case	Convergence Displacement	Experiment (mm)	Model (mm)	Ratio (Model/Experiment)
1	D1	−4.74	−4.43	0.93
	D2	4.68	4.51	0.96
	D3	−6.92	−7.06	1.02
2	D1	−6.37	−7.00	1.10
	D2	8.44	8.72	1.03
	D3	−12.61	−12.34	0.98
3	D1	−1.87	−2.21	1.18
	D2	9.24	9.01	0.98
	D3	−19.68	−18.41	0.94

Figure 11. Measured deformations from experiment and numerical model in Experimental Case 1.

From the comparison of the numerical and experimental results in these three cases with different load levels, it can be concluded that the model established in this paper can evaluate the mechanical behavior of a quasi-rectangular lining structure with good accuracy. The developed model is verified for the quasi-rectangular shield tunnel of Figure 2, whose outline consists of four specific arcs, with ten segments and one interior column. However, the authors are confident that the method considering nonlinear behavior of the joints is applicable for other special-section shield tunnels as well.

4. Discussion of the Results

In previous research on quasi-rectangular tunnels [7,32], the mechanical responses in the tunnel lining were obtained through full-scale ring experiments, but these experiments could not be conducted repeatedly. The verified numerical model presented in this work provides an approach for further structural improvements of the cross-section of quasi-rectangular tunnels. Hereafter, the effects of the incremental method for the joints' rotational stiffness, shear in the circumferential joints and some design parameters are analyzed and discussed through changing the parameter settings in the model.

### 4.1. Comparison between Variable and Constant Rotational Stiffness

In the presented model, the rotational stiffness changes are taken into account through an incremental method, based on experimental and 3D numerical results. In this section, however, constant rotational stiffness values for all segmental joints are used to replace the variable stiffness defined by the incremental method. This allows us to investigate the effect of the incremental method on the bending moments at key sections JM1 to JM10 and the convergence deformations at key deformation points D1 to D3. In the following, a range of constant stiffness values in increments of 25,000 kNm/rad is considered, and the differences between the predicted and experimental values from the indoor full ring experiment are recorded. The evaluations show that only values between 50,000 kNm/rad and 125,000 kNm/rad render reasonably good numerical results, as shown in Figure 12. Results for axial forces in the linings are not presented in this paper, as no significant differences were found between the iterative nonlinear and constant value predictions.

Firstly, considering the bending moments, Figure 12 reveals for a joint stiffness of 125,000 kNm/rad, differences up to 13% in Case 1, up to 15% in Case 2, up to and 36% in Case 3. For the other joint stiffnesses, the maximum differences are 28% (100,000 kNm/rad in Case 3), 19% (75,000 kNm/rad in Case 3), and 21% (50,000 kNm/rad in Case 1). This means that if a reasonable constant stiffness value is used, the bending moment differences can be kept within reasonable limits. However, the differences rise with the increase in pressure level around the tunnel linings, and the constant stiffness fitting the experimental results in the best way, also changes for the different load cases.
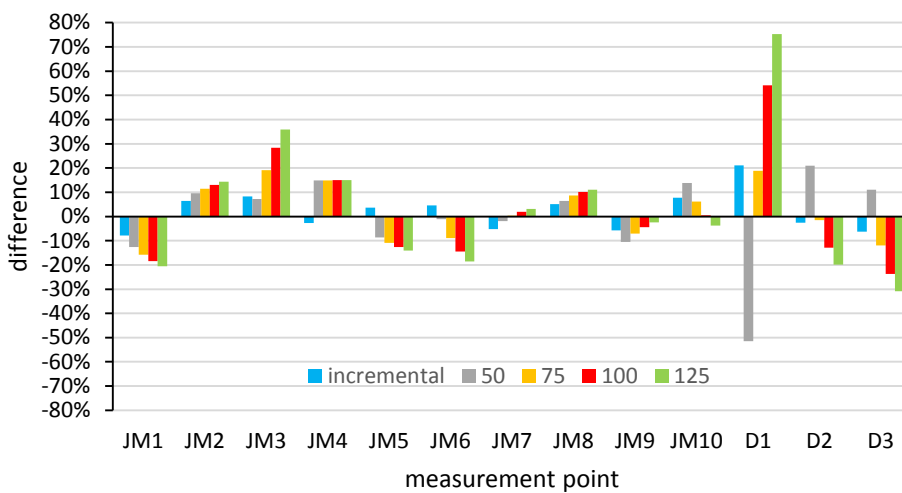
Secondly, considering the key deformations, Figure 12 reveals for a joint stiffness of 125,000 kNm/rad differences up to 11% in Case 1, up to 16% in case 2, and up to 75% in Case 3. For other joint stiffnesses, the maximum differences are 54% (100,000 kNm/rad Case 3), 21% (75,000 kNm/rad Case 1), and 51% (50,000 kNm/rad Case 3).
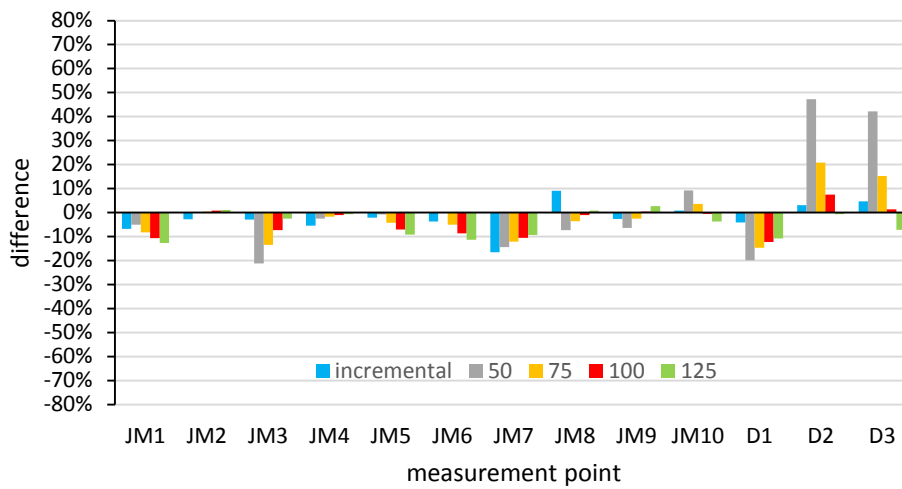
(**a**)
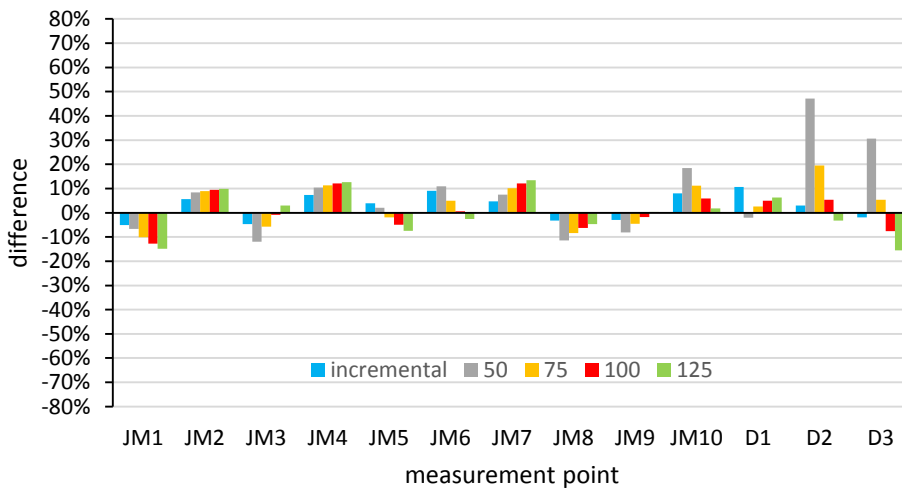
(**b**)

(**c**)

Figure 12. Difference comparison between predictions and experiments: (**a**) Experimental Case 1; (**b**) Experimental Case 2; (**c**) Experimental Case 3 (rotational stiffness in 10^3 kNm/rad).

In contrast to the previous conclusion for the bending moments, it is obvious that the convergence deformations of key deformation points vary significantly with different stiffnesses. This means that the structural deformation is very sensitive to the rotational stiffness input. If the adaption of a constant stiffness value is not supported by full ring tests, the method of constant rotational stiffness in segmental joints may lead to non-negligible deformation prediction errors. On the other hand, the method presented in this paper can consider the joint's nonlinear behavior, and the results obtained by this method can match the experimental results of both deformations and bending moments for all load cases well within the range of about 10% in all but a few measurement points. When the bending moments around the joint's vicinity are large, which may exist in large-diameter and special-section shield tunnels, the joint nonlinear behavior needs to be considered in the calculation model. In general, it can be concluded that a proper constant joint rotational stiffness is difficult to determine, and its deduced deviations may influence the structural design and safety evaluation. The presented incremental method in this paper is able to solve this problem.

4.2. Effect of the Circumferential Joint

4.2.1. Effect of the Circumferential Shear Stiffness

A staggered assembly is commonly adopted in shield tunnel construction [45,46]. Due to the limits of the testing facility, an experiment with a staggered full-scale prototype could not be carried out. In the following section, the effect of staggering is discussed using the incremental model. Herein, the shear stiffnesses in radial and tangential direction are taken into account in the circumferential joints of the model.

The total jack thrust force during the construction of a quasi-rectangular shield tunnel is about 100,000 kN according to the construction data. The longitudinal force in shield tunnels in soft soils is approximately 10–20% of the total thrust of the tunnel boring machine [30,47]. Hereafter, the mean value, i.e., 15%, is adopted. Formula (5) is used to give an estimated value of 288×10^3 kN/m^2 for both the radial and tangential shear stiffnesses. In order to better simulate the real soil and water pressure on the linings, a uniform load distribution is used to replace the point loads in the full-scale ring experiments in Figure 13. Herein, q_1 is the vertical soil and water pressure, q_2 is the ground overload, which is 20 kPa according to Code for Design of Metro [GB50157] [37], q_3 is the bottom counter force, q_4 is the arc-shaped pressure caused by the curve of the linings' outline, g_1 is the structural dead weight, e_1 and e_2 are the lateral pressures, e_3 is the resisting pressure from lateral soils caused by the structural horizontal deformation. The value of q_1 is determined by multiplying the unit weight of the soil by the height of the overburden, and q_3 is balanced by the total load of q_1, q_2 and g_1. The lateral pressure is calculated by multiplying the vertical load with the coefficient of lateral pressure. The lateral soil resisting pressure is calculated by multiplying the structural horizontal deformation with the horizontal coefficient of the soil resistance, which is 6 MPa/m according to tests on the construction site. In previous studies, similar load distributions have been used by Nakamura et al. [5], Lee et al. [14], Hu et al. [15], Li et al. [17], Mo and Chen [48]. Two typical design cases with an 8 and 17 m overburden are used for the analysis in the current study. All relevant parameters are listed in Table 5.

Table 5. Parameters for calculation cases.

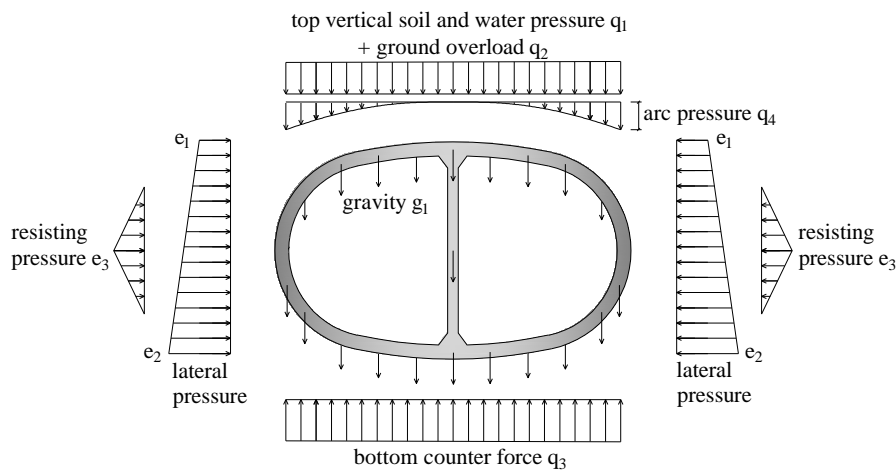| Calculation Case	Soil Overburden (m)	Coefficient of Lateral Pressure	Vertical Soil and Water Pressure q_1 (kPa)	Ground Overload q_2 (kPa)	Bottom Counter Force q_3 (kPa)	Top Value of Lateral Pressure e_1 (kPa)	Bottom Value of Lateral Pressure e_2 (kPa)
1	8	0.7	144.0	20	208.9	114.8	202.7
2	17	0.6	306.0	20	370.9	195.6	271.0

Figure 13. Load distribution for calculation case.

Calculations are made with and without shear stiffness in the circumferential joints. Taking Calculation Case 2 as example, the bending moments on all sections are unfolded clockwise (in the direction of α in Figure 14a) along the circumference and compared in Figure 14. A typical bending moment distribution example is also shown. The joint locations are based on the middle ring (Pattern A) and longitudinal joints JF1 to JF10 and segments in the middle ring are marked, as well as the longitudinal joints of the neighboring rings CJ1 to CJ10. The mean values of the bending moments (green and red curves in Figure 14a) are the average bending moment of a segment section and its related sections in the neighboring rings, namely the average bending moment in the middle ring and its front half ring and back half ring. The bending moment of the middle ring with and without the circumferential shear are illustrated (cyan and black curve in Figure 14b), and the bending moment of the neighboring ring under the condition with circumferential shear is added as well (pink curve in Figure 14b). The bending moments around the joint areas of the interior column and segments T1 and T2 are not shown.
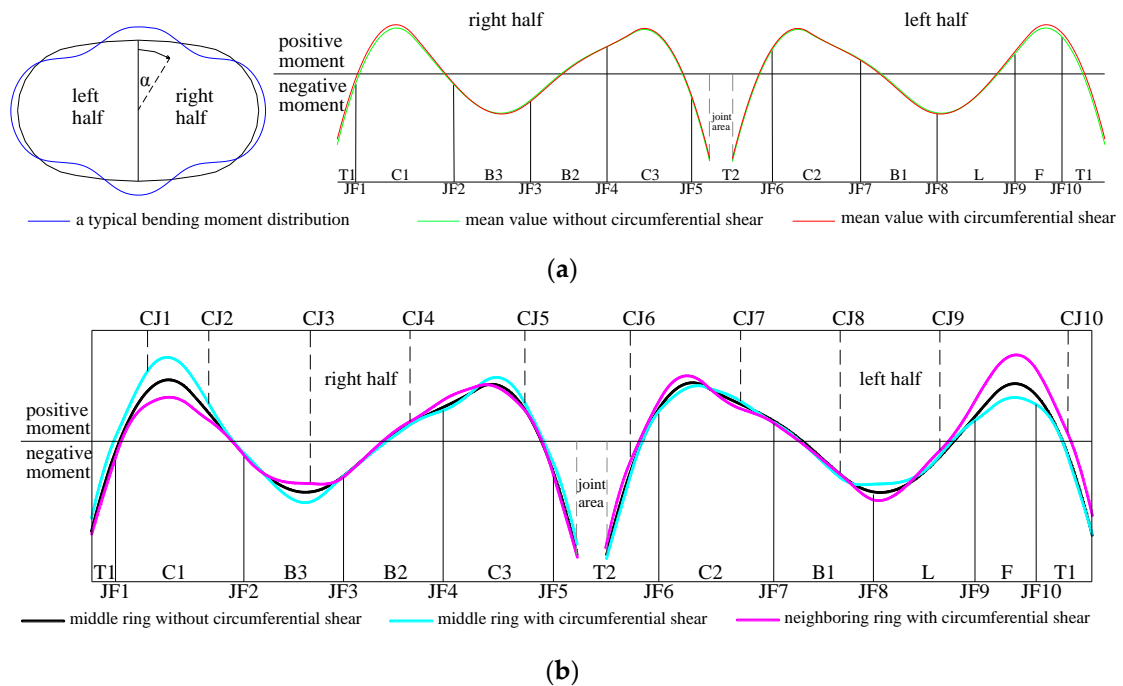

(**a**)

(**b**)

Figure 14. Comparison of bending moment distribution: (**a**) a typical bending moment distribution and mean bending moment values with and without circumferential shear; (**b**) bending moment distribution in different rings.

As shown in Figure 14a, the curves of mean values with and without circumferential shear are in good agreement with each other. This means that the circumferential shear forces have little influence on the overall bending moments in the lining structure model (including all the 3 rings). However, the bending moments on the middle ring appear to have a different distribution, depending on whether the circumferential shear stiffness is considered or not. When comparing the bending moment distribution of the staggered model to that of the model without the circumferential shear in Figure 14b, it is clear that the moment value on the middle ring with circumferential shear stiffness (cyan) is larger than that without circumferential shear stiffness (black). Moreover, the moment on the related section of the neighboring ring (pink) is smaller than that on the middle ring without circumferential shear stiffness (black) and vice versa. It is evident that a transmission of the bending moment occurs because of the existence of the circumferential shear. Comparing the bending moment distributions between the middle and its neighboring rings in the staggered model (cyan and pink), we observe that in the longitudinal joints of the middle ring (JF1 to JF10) with circumferential shear stiffness, the absolute value of the bending moments (cyan) are smaller than those of the neighboring segment bodies (pink), such as JF1, JF2, JF4, JF5, JF6, JF8, JF9, JF10. In the longitudinal joints of the neighboring rings (CJ1 to CJ10), we observe a same situation. This is because the stiffnesses of the longitudinal joints are smaller than those of their neighboring segment bodies. As a result, the bending moments transfer from the weaker area to the stiffer area.

When comparing the left half (segments C2, B1, L, F) of the middle ring with circumferential shear (cyan) to its right half ring (segments C1, B3, B2, C3), it is observed that the moment in the right half ring is generally larger than that in the left half ring, especially at the sections of segment F. This is a direct proof that the right half part of the structure is stiffer than the left half. The cantilever beams of segments T1 and T2 have larger spans in the left half than those in right half (as shown in Figure 2a). The distance between JF6 and JF10 is smaller than that between JF1 to JF5. At the same time, segment F is the smallest segment. All these aspects result in a closer joint layout in the left half, which may be the reason why the right half of the structure is stiffer and a larger bending moment distribution is found in the right half. It also explains that the left convergence deformation (key deformation point of D3) is larger than the right one (key deformation point of D1) in the full-scale ring experiments.

The structure is divided into two parts, left half and right half, by the interior column, and the different stiffnesses in these two parts are a unique characteristic of quasi-rectangular tunnels. It results in a non-symmetric distribution of bending moments in the same ring when the pattern of staggered assembly is adopted. As shown in this case, the bending moment in the neighboring section related to segment F is almost twice the bending moment of segment F.

It should be noted that the phenomenon of bending moment transmission in the staggered assembly will increase the maximum values of positive and negative bending moments in the whole ring, although the bending moments in longitudinal joint sections become smaller which is beneficial for the safety of the joints. Relevant specific measures should be taken for the neighboring segment design, like increasing the amount of reinforcement, in case of possible cracks at the segment bodies due to the bending moment transmission from longitudinal joints in the neighboring rings.

4.2.2. Coefficient of Bending Moment Transmission

In this section, the coefficient of bending moment transmission for a quasi-rectangular tunnel is discussed. The concept for this coefficient is provided by I.T.A. [22] and is commonly used to determine the bending moment distribution between the joints and their neighboring segment bodies [24,41]. As shown in Figure 15 $(1 - \xi) \cdot M$, is taken as the bending moment of the joint section while $(1 + \xi) \cdot M$ is taken as the bending moment of the body section, namely the neighboring segment section. This coefficient is a vital parameter in evaluating the bending moment transmission performance between rings of the staggered segments. It is generally recognized that the coefficient is related to the joint's stiffness, and normally the coefficient ξ is set to 0.3 for a traditional circular tunnel in soft soils [13,49].
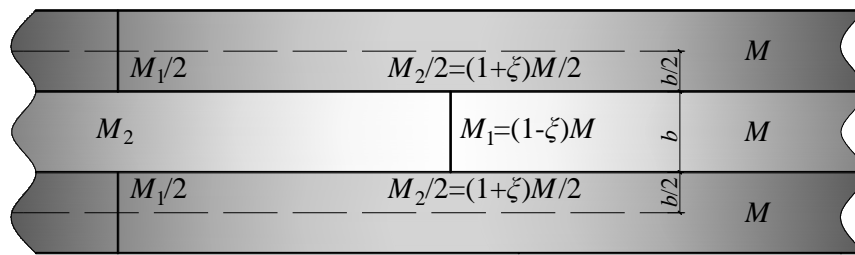
Figure 15. Illustration of bending moment transmission.

According to the Formula (7), ξ can be calculated from Formula (8).

$$\begin{cases} M_1 = (1 - \xi) \cdot M \\ M_2 = (1 + \xi) \cdot M \end{cases} \tag{7}$$

$$\xi = 1 - 2 \cdot M_1 / M_2 \tag{8}$$

The curves of mean bending moments match each other well in Figure 14a, which means that the total bending moments at the joint sections of the middle ring and related neighboring sections with or without circumferential shear stiffness are similar. Therefore, the coefficient of bending moment transmission can be derived to describe the level of bending moment transmission. The bending moment at the joint sections and related neighboring sections are listed in Table 6, as well as the coefficients of bending moment transmission calculated from Formula (8). Additionally, the cases with constant rotational stiffnesses from 100,000 to 400,000 kNm/rad are calculated, and their coefficients of bending moment transmission are also shown to compare the effect of the incremental method. If a range of coefficients of bending moment transmission from constant stiffnesses can cover the corresponding coefficient from the incremental method, the range is underlined for highlighting.

Table 6. Summary of the coefficients of bending moment transmission.

Case	Joint	Incremental Method			ξ						
		Moment (kNm)		ξ	100	150	200	250	300	350	400
		Middle	NEIGHBORING								
	JF1	18	−29	-	-	-	-	-	-	-	-
	JF2	−52	−61	0.09	0.34	0.23	0.17	0.12	0.08	0.05	0.02
	JF3	−67	−72	0.03	0.13	0.09	0.07	0.06	0.05	0.05	0.04
	JF4	60	71	0.08	0.24	0.16	0.11	0.08	0.06	0.04	0.03
	JF5	−53	−82	0.22	0.50	0.38	0.29	0.22	0.16	0.12	0.07
1	JF6	86	107	0.11	0.38	0.25	0.16	0.10	0.06	0.02	0.00
	JF7	38	44	0.07	0.19	0.12	0.09	0.07	0.05	0.05	0.04
	JF8	−106	−136	0.12	0.25	0.17	0.12	0.09	0.06	0.05	0.03
	JF9	26	65	0.43	0.64	0.51	0.41	0.33	0.28	0.23	0.19
	JF10	97	173	0.28	0.35	0.25	0.18	0.14	0.11	0.08	0.06
	JF1	20	−88	-	-	-	-	-	-	-	-
	JF2	−57	−70	0.10	0.45	0.33	0.25	0.19	0.15	0.11	0.08
	JF3	−182	−189	0.02	0.18	0.12	0.09	0.07	0.06	0.05	0.04
	JF4	162	210	0.13	0.28	0.20	0.15	0.11	0.09	0.07	0.05
	JF5	−112	−180	0.23	0.51	0.39	0.31	0.25	0.20	0.16	0.12
2	JF6	176	230	0.13	0.42	0.29	0.20	0.15	0.11	0.07	0.05
	JF7	99	87	-	-	-	-	-	-	-	-
	JF8	−223	−316	0.17	0.26	0.18	0.13	0.10	0.08	0.06	0.05
	JF9	108	196	0.29	0.53	0.42	0.34	0.28	0.24	0.20	0.18
	JF10	190	361	0.31	0.39	0.28	0.22	0.17	0.14	0.11	0.09

The coefficients of bending moment transmission from the incremental method are generally smaller or than 0.3, except for JF9 in Case 1, where a small bending moment exists. This means that the adoption of the coefficient from circular shield tunnels can be proposed. JF9 and JF 10 have the

largest coefficient, and the phenomenon of bending moment transmission reaches a maximum at these joints. The essence of the circumferential shear stiffness is to provide the resisting force for the uneven deformation between neighboring rings [50,51]; the larger the relative stiffness difference between rings, the more pronounced the phenomenon of bending moment transmission. As shown in Figures 2 and 16, the F segment is the smallest segment, and the locations of JF9 and JF10 are close, which means that the area of the F segment is more flexible than other areas in the middle ring and comparatively large deformations may take place here. Besides, its neighboring segment (the segment between CJ9 and CJ10) is the largest segment. Hence, a large stiffness difference exists at the area near the F segment, and the coefficients of bending moment transmission are relatively large. The same explanation is also applicable for the larger coefficient (around 0.23) in JF5, whose neighboring segment (the segment between CJ5 and CJ6) is the neighboring T2 segment, which is well constrained not only by segments but also by the interior column. As can be seen from Table 6, the coefficients of bending moment transmission for different joints of a quasi-rectangular tunnel deviate a lot. These coefficients should be adopted properly based on the location of the joints, especially for JF5, JF9 and JF10.
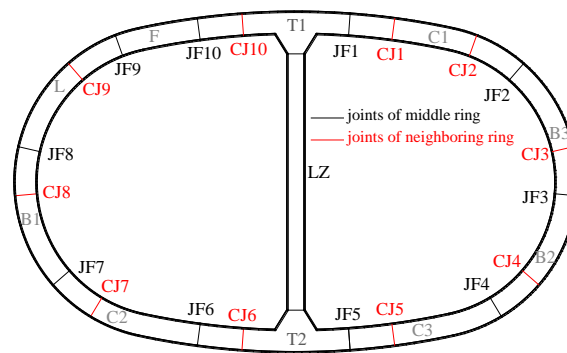

Figure 16. Layout of joints in middle and neighboring rings.

From the calculated coefficients of bending moment transmission, which consider constant rotational stiffnesses, it is obvious that the coefficients decrease with the increase of the constant stiffness values. This is because of the decrease of the stiffness difference between the joint and its corresponding neighboring segment section. Clearly, the coefficients derived from the constant stiffness method, and from the incremental method, deviate a lot. In conclusion, the evaluation of the bending moment transmission phenomenon could be unreliable when using the constant stiffness method, which could possibly result in an unsafe design in practice.

4.3. Parametric Study

The choice for the exact configuration of the longitudinal joints is a critical point in shield tunnel projects [52,53]. It influences the lining's mechanical response, including structural deformations and bending moment distribution, and additionally may affect the safety and applicability of tunnel linings [54–56]. The stiffness of the joint is one of the most important factors for the decision for the joint type [57]. As a new shield tunnel lining structure, the effect of stiffness of the longitudinal joints in quasi-rectangular tunnels is unknown.

The effects of some parameters in the full-ring model, including the rotational and shear stiffnesses of longitudinal joints, and the size of the rigid zone, are discussed here, as well as of the width of the internal column, whose size is also a point of attention in practical applications.

In the parametric study, the values of the parameters are changed to detect the variation tendencies of the structural response. Considering the practical ranges of the parameters, the ranges of the magnification factors for the parametric values are listed in Table 7. When one variable is changed, the other parameters remain constant.

Calculation Case 2 (in Section 4.2), with an overburden of 17 m and a coefficient of lateral pressure of 0.6, is taken as the basis for the parametric study.

Table 7. Ranges of parameters.

Parameter	Range of the Magnification Factors	Value of x
Rotational stiffness	2^x	$\pm4, \pm3, \pm2, \pm1, 0$
Shear stiffness	2^x	$\pm4, \pm3, \pm2, \pm1, 0$
Size of rigid zone	0 and 2^x	$\pm2, \pm1, 0$
Width of interior column	2^x	$-2, -1, 0, 1$

The calculation results of the deformation at D3 and the bending moments at JM2, JM8 and JM10 (shown in Figure 17) are selected as the target objects to detect the effect of the aforementioned parameter variations. The choice is determined by the observation that in Calculation Case 2, the largest deformations take place at D3 while JM2 and JM10 are the sections with the largest positive and negative bending moment respectively. Additionally, relatively large negative moments also occur at the ends of the long axis at JM3 and JM8 (Figure 6). The deformations and internal forces at these sections act as the main controlling factors for the structural design.
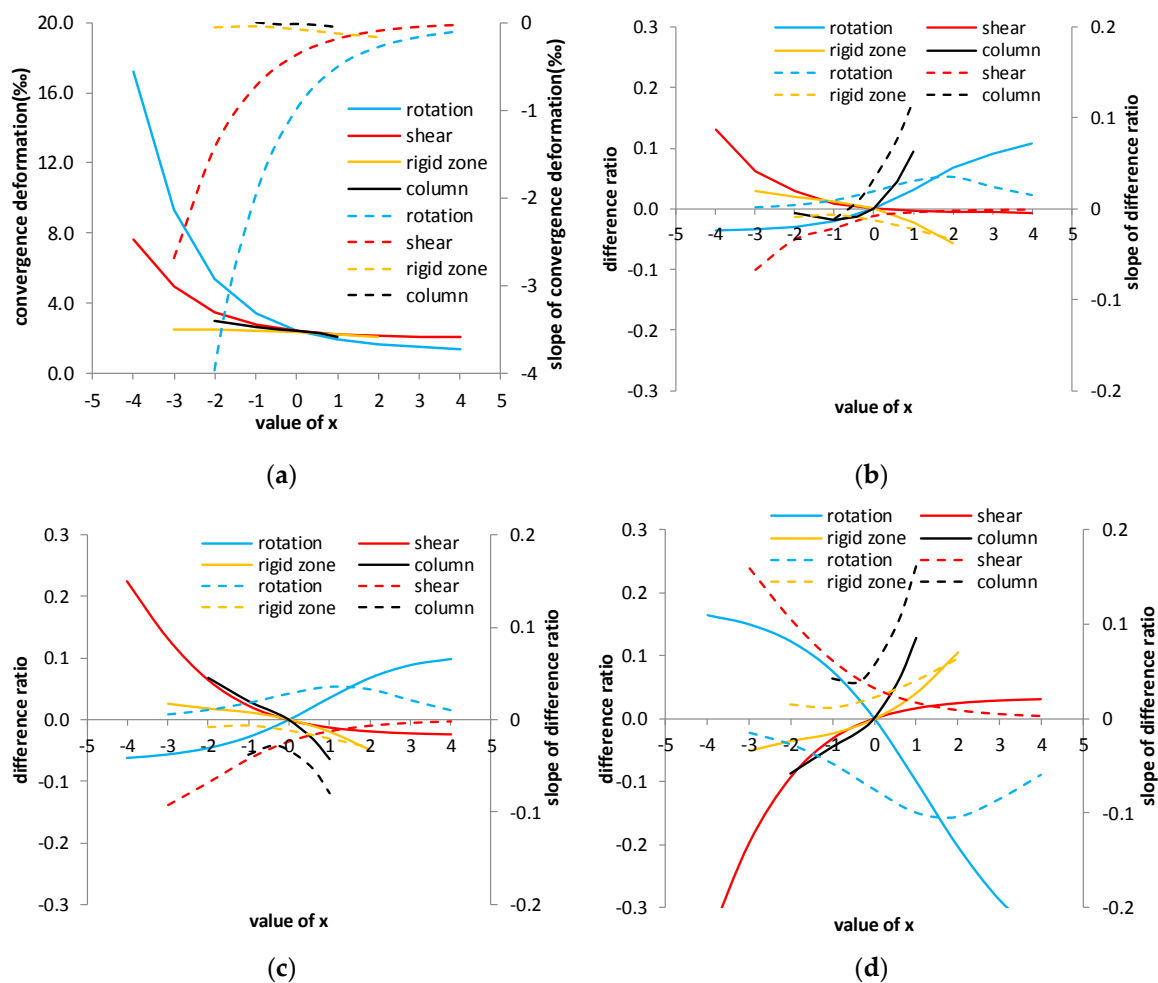

Figure 17. Results of parameter analysis: (**a**) deformation of D3; (**b**) bending moment at JM2; (**c**) bending moment at JM8; (**d**) bending moment at JM10.

In the graphs presented in Figure 17, the exponent "x" is the variable on the abscissa axis. The value of the corresponding input parameter is multiplied by 2^x. The contrasts of the results with the magnified or reduced parameters to the results with the original parameters are shown in full lines with the left ordinate axes. In Figure 17a, the convergence deformation is calculated by dividing the deformation of D3 by the original length of D3, while the difference ratios of the bending moments at JM2, JM8 and JM10 to those with the original parameter settings are summarized in Figure 17b–d. Moreover, the slopes of these curves are calculated, equivalent to the change rate of the selected target objects, and are shown in dashed lines with reference to the right axes.

The reader should pay attention to the magnification factor of 0 in the row of "size of rigid zone" in Table 7. The "0" indicates that there is no rigid zone in the model, and the related "x" is taken as −3 in Figure 17, in order to compare with the actual range of "x" from −2 to 2.

By definition, in these dashed curves, the positive values mean that the target object increases in absolute value with the increase of the magnification factors, while the negative values mean opposite tendencies. These tendencies are hereafter represented by ↑ and ↓, respectively. The values in the dashed curves represent the change rate (positive or negative), i.e., the level of sensitivity to the relative parameter. Target objects which are very sensitive to a certain parameter are indicated using ↑↑ or ↓↓. Based on the calculation results, the tendencies and the levels of sensitivity to the parameters are summarized in Table 8.

According to the summary, optimizing the structural performance by adjusting only one parameter is difficult, as increasing the value of one parameter never decreases the absolute values of all target objects. A combination of the choices for the parameters is significant for practical design in order to obtain a better structural response.

Table 8. Summary of the tendency and sensitive level of different parameters.

Target Object	D3 (Max of Deformation)	JM2 (Max of Positive Moment)	JM8 (Max1 of Negative Moment)	JM10 (Max2 of Negative Moment)
Rotation	↓↓	↑	↑	↓↓
Shear	↓↓	↓	↓↓	↑↑
Rigid zone	↓	↓	↓	↑
Column	↓	↑↑	↓↓	↑↑

As shown in Table 8, the shear stiffness and the width of the column play an important role in the design of quasi-rectangular tunnel linings. Shear stiffness does not affect the behavior of circular shield tunnels significantly as smaller shear forces exist in circular tunnels. However, when it comes to quasi-rectangular tunnels, due to the shape of the section and the existence of the interior column, the shear forces influence a lot both the structural deformations as the maximum bending moments. The column is the unique characteristic in the design of this type of tunnel, and its width influences the bending moments to a large extent. Therefore, considerable attention needs to be paid to the shear stiffness and the size of the interior column. It is worth mentioning that a change of the size of the rigid zone results in a difference of 10% of maximum bending moments. As such, a choice for the suitable area of the rigid zone also needs due attention.

5. Conclusions

The stiffnesses of the joints in a shield tunnel are related to the level of the joints' internal forces. For joints in quasi-rectangular tunnels, the joints' rotational and shear deformations are not only affected by bending moments and shear forces in the joints but also by axial forces. Additionally, the longitudinal joints of quasi-rectangular tunnels are subjected to a wide range of both bending moments and shear forces. Considering this, a proper numerical model is required for the further study and structural improvement of this new type of tunnel.

(1) In this paper an iterative incremental method is presented to simulate the stiffness changes caused by the joint's moment-axial force and shear-axial force interaction behavior. The applicability of the numerical model is verified by comparing the bending moments and deformations in the lining to the results of unique indoor full-scale ring experiments;

(2) The iterative incremental method provides acceptable results for different load levels, while a constant stiffness based analysis does not;

(3) Investigation of the effect of the circumferential shear stiffness reveals that the half part of the tunnel lining without the smallest segment (F in Figure 2) is stiffer than the other half. Consequently, in tunnels with a staggered assembly, the bending moments in this half part increase a lot, almost doubling the bending moment in the F segment, due to the bending moment transmission caused by the uneven deformation in these two halves;

(4) The range of the coefficients of bending moment transmission for the joints in a quasi-rectangular tunnel is similar to that of circular shield tunnels, but between each other, they deviate significantly. Consequently, they should be adopted properly, based on the location of the joints, and especially relatively large transmission coefficient values up to 0.3 are needed for the joints at the edges of the smallest segment (JF9 and JF10 in Figure 2);

(5) A parametric study reveals that not only the joint's rotational stiffness but also the width of interior column and the joint's shear stiffness significantly affect the structural response. Optimizing the structural performance by adjusting only one parameter is difficult. A combination of the choices for the parameters is significant for practical design of quasi-rectangular tunnel linings.

(6) For circular tunnels, only one geometric shape has to be considered. However, for quasi-rectangular tunnels, many geometric shapes are possible. Although the analysis presented in this paper is based on the particular geometry of a metro tunnel in Ningbo, the conclusions could be helpful for other special-section shield tunnels as well, especially where the influence of the nonlinear behavior of the joints is non-negligible.

Appendix A

The joint specimens used in the bending moment resistance experiments are full-scale and specifically cast for the joint experiments. As shown in Figure A1, the joint specimens are linear, rather than curved segments in order to get precise bending moment values, since according to Zhang et al. [58], the mechanics in the joint of curved and linear lining segments can be considered equal. A specimen is composed of two segments connected by two pairs of cast iron embedded parts (Figure A3). The size of each segment is $1250 \times 1200 \times 450$ mm. Four 6.8-M33 short straight bolts connect the cast iron parts. The ends of the segments are put into steel loading supports, and the gaps are filled with steel plates to ensure the segments are tied to the loading supports. A set of horizontal hinged jacks on the right side provide the axial force through pushing on the loading supports. A steel roller constrains the displacement of the left loading support, but the rotational movement is allowed. Two bottom rollers under the loading supports only balance the vertical force and allow the supports to rotate freely. The bending moment is exerted through a vertical jack and a set of distribution beams.
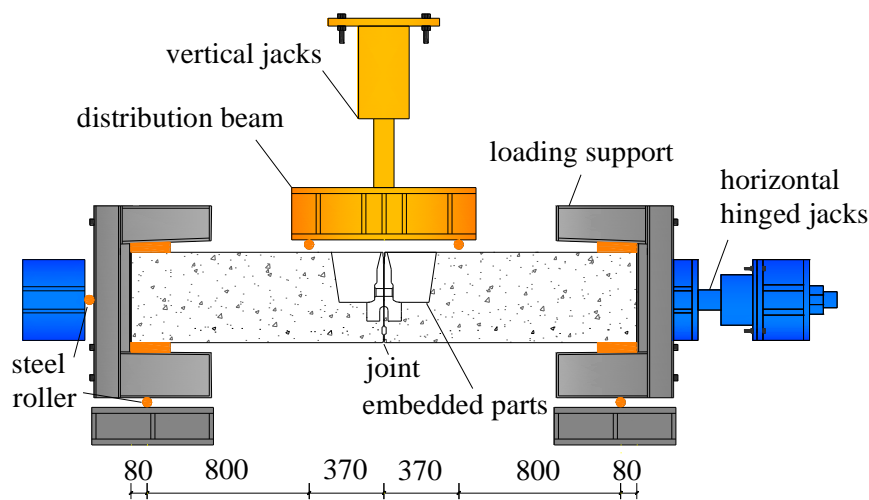
Figure A1. View of specimen and loading device for bending moment resistance experiment.

The horizontal jacks and vertical jacks provide axial force N and vertical load P. P_c is the reaction force from the loading support and is equal to the sum of the vertical load P and the dead weight G. The distances between different loads are known, and thus, the bending moment at the joint can be calculated as shown in Figure A2. The axial force N and vertical load P can be adjusted through an electro-hydraulic servo loading system to make the internal forces in the joints equal to target values.
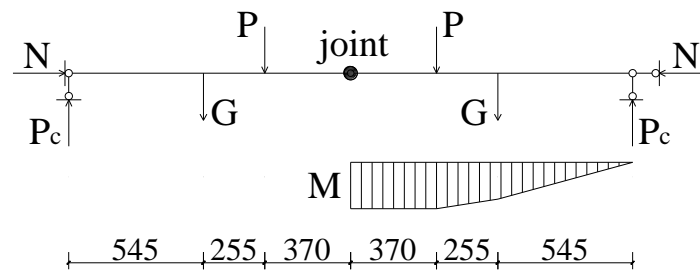

Figure A2. Illustration of bending moment calculation.

A refined nonlinear 3D finite element model is used to obtain the joint's deformation and provide load dependent stiffness values needed in the proposed quasi-rectangular tunnel lining numerical model. An ABAQUS [2018] 3D model of a linear segment including all geometrical details is created. The tested segment is shown in Figure A3a. Considering the symmetry of the specimen in the numerical model, only 1/2 of one joint segment is modelled to save calculation time. Half of the concrete segment, a single cast iron embedded part, two bolts, and two bolting pads are constructed as shown in Figure A3b. Symmetric displacement constraints are applied to consider the other half of the concrete segment. The other segment is modelled by a symmetry condition represented by a rigid plate and contact conditions allowing for separation as shown in Figure A3c. The reinforcement cage is also taken into account in the model. Due to the complexity and irregularity of the embedded parts and geometric details, 280,000 elements are meshed. The fine mesh is targeted at the joint section and the embedded part with the finest size of 7 mm while the coarse mesh is at the far end of the specimen.

For the concrete, the concrete damage plasticity model is used, while for the steel a multi-linear elastoplastic model is used. Further information about the FE model and the comparative results can be found in reference [33].
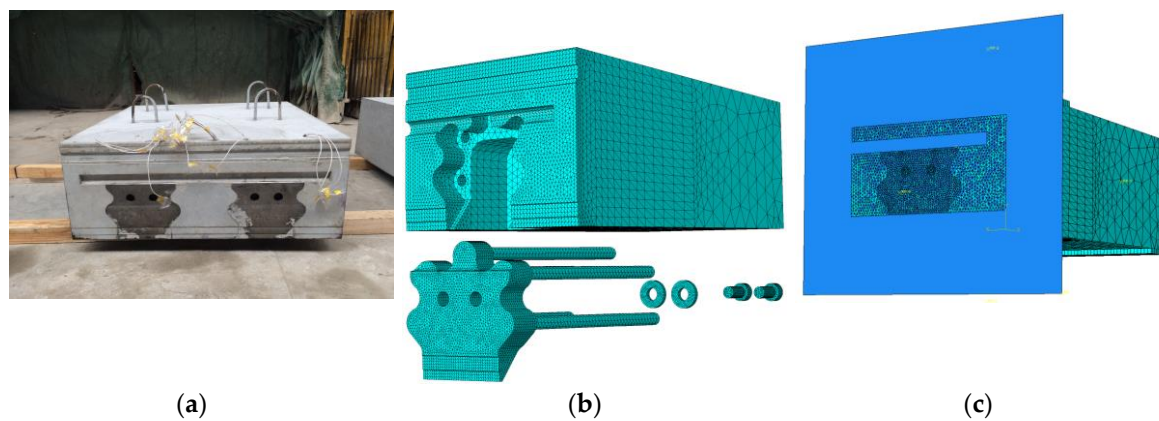
(**a**)   (**b**)   (**c**)

Figure A3. Tested joint segment and joint 3D model: (**a**) tested joint segment; (**b**) half of the concrete segment, embedded part, bolts and bolting pads; (**c**) model after assembly.

Appendix B

Full-scale shear resistance experiments are carried out to retrieve the joint's shear stiffness under different compressive forces as shown in Figure A4. A tested specimen is composed of 3 segments. The ends of the segments are clamped by steel loading supports, and a set of horizontal jacks on the right side exert compressive forces. Two bottom rollers under the loading supports only sustain the vertical force for balancing the force from the vertical jack. The vertical jacks produce shear forces at the two joints. In order to avoid bending moments at the joints produced by the shear forces, the action points of the distribution beam and the steel rollers are arranged very close to each other in the horizontal direction. In each case, the compressive force from the horizontal jack is kept at target values (500, 583, 667, 750 and 833 kN/m), and the vertical load is increased in order to investigate the shear stiffnesses under different compressive forces. The shear stiffness can be calculated by dividing the joint's dislocation by the related shear force at the joint.
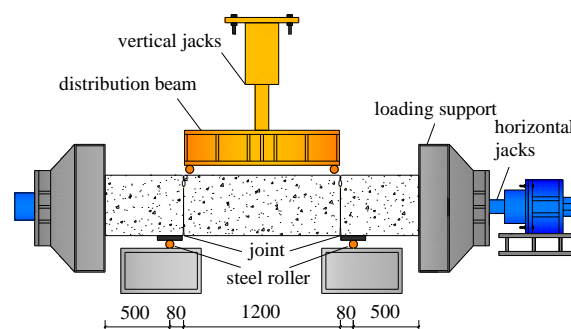

Figure A4. View of specimens and loading device for shear resistance experiment.

References

1. Zhu, Y.; Zhu, Y.; Huang, D.; Li, P. Development and application of the technical system for quasi-rectangular shield tunnelling. *Mod. Tunn. Technol.* **2016**, *53*, 1–12. [CrossRef]
2. Liu, X.; Liu, Z.; Yuan, Y.; Zhu, Y. Quasi-Rectangular Shield Tunneling Technology in the Ningbo Rail Transit Project. *High Tech. Concrete Where Technol. Eng. Meet* **2018**, 2765–2773. [CrossRef]
3. Liu, X.; Ye, Y.; Liu, Z.; Huang, D. Mechanical behavior of Quasi-rectangular segmental tunnel linings: First results from full-scale ring tests. *Tunn. Undergr. Space Technol.* **2018**, *71*, 440–453. [CrossRef]
4. Chow, B. Double-O-tube shield tunneling technology in the Shanghai Rail Transit Project. *Tunn. Undergr. Space Technol.* **2006**, *21*, 594–601. [CrossRef]
5. Ye, G.; Hashimoto, T.; Shen, S.; Zhu, H.; Bai, T. Lessons learnt from unusual ground settlement during Double-O-Tube tunnelling in soft ground. *Tunn. Undergr. Space Technol.* **2015**, *49*, 79–91. [CrossRef]

6. Nakamura, H.; Kubota, T.; Furukawa, M.; Nakao, T. Unified construction of running track tunnel and crossover tunnel for subway by rectangular shape double track cross-section shield machine. *Tunn. Undergr. Space Technol.* **2003**, *18*, 253–262. [CrossRef]

7. Sun, W.; Guan, L.; Wen, Z. Mechanical analysis and application of large rectangular cross-section shield tunnel. *Tunn. Construct.* **2015**, *35*, 1028.

8. Morgan, H. A contribution to the analysis of stress in a circular tunnel. *Geotechnique* **1961**, *11*, 37–46. [CrossRef]

9. Tang, Y. The Mechanism Study of the Staggering Assembly of Shield-Driven Tunnel. Master's Thesis, Tongji University, Shanghai, China, 1988.

10. Peck, R.B.; Hendron, A.; Mohraz, B. State of the art of soft-ground tunneling. In Proceedings of the North American Rapid Excavation and Tunneling Conference, Chicago, IL, USA, 5–7 June 1972; pp. 259–286.

11. Wood, A.M. The circular tunnel in elastic ground. *Geotechnique* **1975**, *25*, 115–127. [CrossRef]

12. Liu, J.; Hou, X. *Shield Driven Tunnel*; China Railway Publishing House: Bejing, China, 1991.

13. Koyama, Y. Present status and technology of shield tunneling method in Japan. *Tunn. Undergr. Space Technol.* **2003**, *18*, 145–159. [CrossRef]

14. Lee, K.; Hou, X.; Ge, X.; Tang, Y. An analytical solution for a jointed shield-driven tunnel lining. *Int. J. Numer. Anal. Methods Geomech.* **2001**, *25*, 365–390. [CrossRef]

15. Hu, X.; Zhang, Z.; Teng, L. An analytical method for internal forces in DOT shield-driven tunnel. *Tunn. Undergr. Space Technol.* **2009**, *24*, 675–688. [CrossRef]

16. Li, Z.; Soga, K.; Wang, F.; Wright, P.; Tsuno, K. Behaviour of cast-iron tunnel segmental joint from the 3D FE analyses and development of a new bolt-spring model. *Tunn. Undergr. Space Technol.* **2014**, *41*, 176–192. [CrossRef]

17. Li, Z.; Soga, K.; Wright, P. Behaviour of cast-iron bolted tunnels and their modelling. *Tunn. Undergr. Space Technol.* **2015**, *50*, 250–269. [CrossRef]

18. Lei, M.; Lin, D.; Shi, C.; Ma, J.; Yang, W. A Structural Calculation Model of Shield Tunnel Segment: Heterogeneous Equivalent Beam Model. *Adv. Civ. Eng.* **2018**, *2018*. [CrossRef]

19. Lee, K.; Ge, X. The equivalence of a jointed shield-driven tunnel lining to a continuous ring structure. *Can. Geotech. J.* **2001**, *38*, 461–483. [CrossRef]

20. Klappers, C.; Grübl, F.; Ostermeier, B. Structural analyses of segmental lining–coupled beam and spring analyses versus 3D-FEM calculations with shell elements. *Tunn. Undergr. Space Technol.* **2006**, *21*, 254–255. [CrossRef]

21. Teachavorasinskun, S.; Chub-uppakarn, T. Influence of segmental joints on tunnel lining. *Tunn. Undergr. Space Technol.* **2010**, *25*, 490–494. [CrossRef]

22. International Tunnelling Association. Guidelines for the design of shield tunnel lining. *Tunn. Undergr. Space Technol.* **2000**, 303–331. [CrossRef]

23. Ding, W.; Yue, Z.; Tham, L.; Zhu, H.; Lee, C.; Hashimoto, T. Analysis of shield tunnel. *Int. J. Numer. Anal. Methods Geomech.* **2004**, *28*, 57–91. [CrossRef]

24. Ye, F.; Gou, C.-f.; Sun, H.-d.; Liu, Y.-p.; Xia, Y.-x.; Zhou, Z. Model test study on effective ratio of segment transverse bending rigidity of shield tunnel. *Tunn. Undergr. Space Technol.* **2014**, *41*, 193–205. [CrossRef]

25. Li, X.; Yan, Z.; Wang, Z.; Zhu, H. Experimental and analytical study on longitudinal joint opening of concrete segmental lining. *Tunn. Undergr. Space Technol.* **2015**, *46*, 52–63. [CrossRef]

26. Majdi, A.; Ajamzadeh, H.; Nadimi, S. Investigation of moment-rotation relation in different joint types and evaluation of their effects on segmental tunnel lining. *Arab. J. Geosci.* **2016**, *9*, 512. [CrossRef]

27. Jin, Y.; Ding, W.; Yan, Z.; Soga, K.; Li, Z. Experimental investigation of the nonlinear behavior of segmental joints in a water-conveyance tunnel. *Tunn. Undergr. Space Technol.* **2017**, *68*, 153–166. [CrossRef]

28. Blom, C.B.M. Design Philosophy of Concrete Linings for Tunnels in Soft Soils. Ph.D. Thesis, Delft University of Technology, Delft, The Netherlands, 2004.

29. Zhong, X.; Zhu, W.; Huang, Z.; Han, Y. Effect of joint structure on joint stiffness for shield tunnel lining. *Tunn. Undergr. Space Technol.* **2006**, *21*, 406–407. [CrossRef]

30. Arnau, O.; Molins, C.; Blom, C.; Walraven, J. Longitudinal time-dependent response of segmental tunnel linings. *Tunn. Undergr. Space Technol.* **2012**, *28*, 98–108. [CrossRef]

31. International Tunnelling Association. *Twenty Years of FRC Tunnel Segment Practice: Lessons Learned and Proposed Design Principles*; I.T.A. Working Group NO.2: Avignon, France, 2016.

32. Liu, X.; Liu, Z.; Ye, Y.; Bai, Y.; Zhu, Y. Mechanical behavior of quasi-rectangular segmental tunnel linings: Further insights from full-scale ring tests. *Tunn. Undergr. Space Technol.* **2018**, *79*, 304–318. [CrossRef]

33. Zhang, W.; Liu, X.; De Corte, W.; Taerwe, L. Investigation of the rotational stiffness of longitudinal joints in quasi-rectangular segmental tunnel linings. In Proceedings of the Fib Symposium 2019: Concrete—Innovations in Materials, Design and Structures, Krakow, Poland, 27–29 May 2019.

34. Zhu, Y.; Zhang, Z.; Huang, X.; Zhu, Y. Numerical Investigation on the Mechanical Characteristics of a Special-Shaped Shield Lining with a Large Cross-Section. In Proceedings of the GeoShanghai International Conference, Shanghai, China, 27–30 May 2018.

35. *Code for Design of Concrete Structures [GB50010]*; Ministry of Housing and Urban-Rural Development of the People's Republic of China (MOHURD): Beijing, China, 2011. (In Chinese)

36. *Technical Specification for Concrete Structure of Tall Building [JGJ3-2010]*; Ministry of Housing and Urban-Rural Development of the People's Republic of China (MOHURD): Beijing, China, 2011. (In Chinese)

37. *Code for Design of Metro [GB50157]*; Ministry of Housing and Urban-Rural Development of the People's Republic of China (MOHURD): Beijing, China, 2013. (In Chinese)

38. Blom, C.; Van der Horst, E.; Jovanovic, P. Three-dimensional structural analyses of the shield-driven "Green Heart" tunnel of the high-speed line south. *Tunn. Undergr. Space Technol.* **1999**, *14*, 217–224. [CrossRef]

39. Schreyer, J.; Winselmann, D. Suitability tests for the lining for the 4th Elbe tunnel tube–Results of large-scale tests. *Tunnel* **2000**, *1*, 34–44.

40. Lu, L.; Lu, X.; Fan, P. Full-ring experimental study of the lining structure of Shanghai Changjiang tunnel. In Proceedings of the 4th International Conference on Earthquake Engineering, Thessaloniki, Greece, 25–28 June 2007.

41. Huang, X.; Liu, W.; Zhang, Z.; Wang, Q.; Wang, S.; Zhuang, Q.; Zhu, Y.; Zhang, C. Exploring the three-dimensional response of a water storage and sewage tunnel based on full-scale loading tests. *Tunn. Undergr. Space Technol.* **2019**, *88*, 156–168. [CrossRef]

42. Moriya, Y. Special shield tunneling methods in Japan. In Proceedings of the International Conference on Tunnels and Underground Structures, Singapore, 26–29 November 2000; pp. 225–249.

43. Liu, X.; Dong, Z.; Bai, Y.; Zhu, Y. Investigation of the structural effect induced by stagger joints in segmental tunnel linings: First results from full-scale ring tests. *Tunn. Undergr. Space Technol.* **2017**, *66*, 1–18. [CrossRef]

44. Liu, X.; Bai, Y.; Yuan, Y.; Mang, H.A. Experimental investigation of the ultimate bearing capacity of continuously jointed segmental tunnel linings. *Struct. Infrastruct. Eng.* **2016**, *12*, 1364–1379. [CrossRef]

45. Gil Lorenzo, S. *Structural Behaviour of Concrete Segmental Lining Tunnels: Towards Design Optimisation*; University of Cambridge: Cambridge, UK, 2018.

46. Arnau Delgado, O. Structural response of precast concrete segmental tunnel linings. Ph.D. Thesis, Universitat Politècnica de Catalunya, Catalunya, Spain, 2012.

47. Galván, A.; Peña, F.; Moreno-Martínez, J.Y. Effect of TBM advance in the structural response of segmental tunnel lining. *Int. J. Geomech.* **2017**, *17*, 04017056. [CrossRef]

48. Mo, H.; Chen, J. Study on inner force and dislocation of segments caused by shield machine attitude. *Tunn. Undergr. Space Technol.* **2008**, *23*, 281–291. [CrossRef]

49. JSCE. *Japanese Standard for Shield Tunneling*; Zhu, W., Translator; Japan Society of Civil Engineers, China Construction Industry Press: Beijing, China, 2001. (In Chinese)

50. Liu, X.; Zhang, C.; Zhang, C.; Yuan, Y. Ultimate load-carrying capacity of the longitudinal joints in segmental tunnel linings. *Struct. Concr.* **2017**, *18*, 693–709. [CrossRef]

51. Liu, X.; Dong, Z.; Song, W.; Bai, Y. Investigation of the structural effect induced by stagger joints in segmental tunnel linings: Direct insight from mechanical behaviors of longitudinal and circumferential joints. *Tunn. Undergr. Space Technol.* **2018**, *71*, 271–291. [CrossRef]

52. Yan, Z.; Peng, Y.; Ding, W.; Zhu, H.; Huang, F. Load tests on segment joints of single lining structure of shield tunnel in Qingcaosha water conveyance project. *Chin. J. Geotech. Eng.* **2011**, *33*, 1385–1390.

53. Caratelli, A.; Meda, A.; Rinaldi, Z.; Giuliani-Leonardi, S.; Renault, F. On the behavior of radial joints in segmental tunnel linings. *Tunn. Undergr. Space Technol.* **2018**, *71*, 180–192. [CrossRef]

54. Zhang, J.L.; Mang, H.A.; Liu, X.; Yuan, Y.; Pichler, B. On a nonlinear hybrid method for multiscale analysis of a bearing-capacity test of a real-scale segmental tunnel ring. *Int. J. Numer. Anal. Methods Geomech.* **2019**. [CrossRef]

55. Gruebl, F. Segmental Ring Design: New Challenges with High Tunnel Diameters. *TAI J.* **2012**, *1*, 4–9.

56. Koyoma, Y.; Nishimura, T. *The Design of Lining Segment of Shield Tunnel Using a Beam-Spring Model*; Railway Technical Research Institute: Kokubunji-shi, Tokyo, Japan, 1998; p. 39.

57. Li, X.; Yan, Z.; Wang, Z.; Zhu, H. A progressive model to simulate the full mechanical behavior of concrete segmental lining longitudinal joints. *Eng. Struct.* **2015**, *93*, 97–113. [CrossRef]

58. Zhang, H.; Fu, D.; Guo, C. Study on load test of segment joint in shield driven tunnel. *Mod. Tunn. Technol.* **2002**, *39*, 28–34.